Available online at www.sciencedirect.com

jmr&t Journal of Materials Research and Technology

journal homepage: www.elsevier.com/locate/jmrt

Original Article

The influence of V addition on the structure, mechanical properties, and oxidation behaviour of TiAlSiN coatings deposited by DC magnetron sputtering

A. AL-Rjoub [a,*], Talha Bin Yaqub [a,b], A. Cavaleiro [a,b], F. Fernandes [a,b,c]

[a] University of Coimbra, CEMMPRE - Centre for Mechanical Engineering Materials and Processes, Department of Mechanical Engineering, Rua Luís Reis Santos, 3030-788 Coimbra, Portugal

[b] IPN - LED$ MAT - Instituto Pedro Nunes, Laboratório de Ensaios, Desgaste e Materiais, Rua Pedro Nunes, 3030-199 Coimbra, Portugal

[c] ISEP - School of Engineering, Polytechnic of Porto, Rua Dr. António Bernardino de Almeida 431, 4200-072 Porto, Portugal

ARTICLE INFO

Article history:
Received 30 May 2022
Accepted 2 August 2022
Available online 13 August 2022

Keywords:
TiAlSiVN films
Structure
Oxidation resistance

ABSTRACT

The influence of V content on the morphology, structure, hardness (H) and reduced Young's modulus (E), adhesion, and oxidation resistance of TiAlSiN coatings is investigated. The coatings were produced by DC reactive magnetron sputtering, with increasing V contents from 0, 4.8 and 11.0 at.%. All coatings exhibit a fcc type structure. The coating with 4.8 at.% of V shows the highest values of H and E, whereas the values are similar for the reference coating and the coating with 11.0 at.% of V. The coatings adhere well to the substrates and show a dense and compact columnar growth extending from the adhesive interlayer to the top surface of the coatings. The dynamic thermal gravimetric oxidation curves reveal that V additions decreases the onset point of oxidation significantly and degrades the oxidation resistance of the coatings. A dual oxide layer is formed on the top surface of the reference coating: an outer porous Ti–Al–O rich layer with plate-like features on the top, which classified to TiO_2 (rutile and anatase) and Al_2O_3 phases, and an inner Ti–Si–O rich layer with Al depletion that identified as mixture of amorphous Si–O and Ti–Si–O protective oxides. The diffusion of V to the top surface governs the oxidation process of the V-containing coatings, i.e. increasing V concentration leads to disrupt the formation of the protective continuous oxide layers easily.

* Corresponding author.
E-mail address: abbas.al-rjoub@dem.uc.pt (A. AL-Rjoub).

https://doi.org/10.1016/j.jmrt.2022.08.009

1. Introduction

As reported in the literature, Magnéli oxide phases (transition metal binary oxides) [1] have been widely used in the protective coatings for high-speed cutting and dry machining processes in the last century. These phases are oxides of transition metals such as Ti, V, W, or Mo named after the Swedish scientist Arne Magnéli who investigated their structure for the first time in literature [1,2]. The easy low crystallographic shear planes with reduced binding strength of these oxides make them perfect candidates for solid lubricant agents in the dry machining. Therefore, the lubricious nature of these oxides decreases the friction and enhances the wear performance during machining at high temperatures, attributing to the defect structure associated with the formation of sub-stoichiometric compound, and eliminating the environmental harmful lubrication [3–6].

In particular, the formation of low melting point lubricious Magnéli V_nO_{3n-1} phases in V- alloyed coating systems have been intensively reported in literature due to their interesting tribological properties in the temperature range 500–700 °C (e.g. the monolayered nanostructure of AlCrSiVN [7], AlCrVN [8], TiAlVSiCN [9], TiAlVN [10], VN [3], CrVN [11], VSiN [12] VCN–Ag [13], TiSiVN [14–17]) or multilayered coating systems as TiN/VN [18] TiSiN/VN [19], TiSiN/CrVN [20], CrAlSiN/TiVN [21], TiAlVN/TiAlSiN [22], and TiAlN/VN [23–25]). Vanadium incorporation into transition metals nitrides causes the rapid oxidation of the coating at elevated temperatures, and enables the formation of the lubricious oxides, resulting in a decrease in the COF and a better wear resistance [2]. This will improve the tribological performance of the coating under dry machining conditions at high temperatures [26]. However, vanadium degrades the oxidation resistance of V-alloyed nitrides coatings and allows the fast release of the oxide lubricious phase. Therefore, the control of this fast release is still needed to provide the long-term lubrication and to meet the high-speed cutting and dry machining processes at high temperatures conditions [2,6,15,20]. In our previous studies [4,16,17], we investigated the role of a-SiNx in controlling the fast release of the lubricious phase together with the enhancement of the oxidation resistance of magnetron sputtered TiSiVN coatings. We reported that a-SiNx could provide better barriers against the fast release of vanadium oxides lubricant phase, and it improves the oxidation resistance compared with the TiVN coatings.

In the current work, the effect of V addition on the morphology, structure, hardness (H) and reduced Young's modulus (E), adhesion, and oxidation resistance of TiAlSiN coatings deposited by D.C. reactive magnetron sputtering is investigated.

2. Experimental

TiAlSiVN coatings with different V contents were deposited by DC reactive magnetron sputtering in a chamber containing two cathodes positioned perpendicularly to each other. Ti and Cr high-purity (99.9%) targets (150 × 150 × 8 mm) were used in the depositions. The Ti target has 20 holes of 10 mm in diameter, distributed uniformly in the target erosion zone, was filled with 6 Si and 7 Al pellets, being the remaining holes were filled with 0, 3, and 6 V-pellets to produce the reference coating (C_0) TiAlSiN, TiAlSiVN (C_1) with 4.8 at% V, and TiAlSiVN (C_2) with 11.0 at% V coatings, respectively. Three types of substrates were used in the depositions: i) FeCrAlY alloy (12 × 8 × 1 mm), to assess the coating's hardness, reduced Young's modulus, structure, morphology, thickness and chemical composition, ii) Al_2O_3 (10 × 8 × 0.5 mm) for oxidation resistance tests, and iii) M_2 stainless steel substrates were used for the scratch tests.

The substrates were ultrasonic cleaned in acetone and in alcohol for 15 and 10 min, respectively. Then, they were mounted on the substrate holder placed at the centre of the deposition chamber. The chamber was vacuumed down to the base pressure of 3×10^{-4} Pa and the substrates were etched for 40 min in Ar atmosphere (pulsed bias of −230 V and frequency of 250 kHz). At the same time, the two targets were shuttered and cleaned/sputtered for 20 min. An interlayer and a gradient layer were deposited to improve the adhesion of the coatings. The interlayer was grown by applying a power density of

Table 1 – Deposition parameters and main properties of the coating.

Sample		C_0	C_1	C_2
The number of V rods in the Ti target		0	3	6
The power density of TiAlSiV target (W/cm^2)		6.7	6.7	6.7
The power density of Cr target (W/cm^2) for interlayer		5.3	5.3	5.3
Rotation speed (rotation/min)		20	20	20
Deposition time of the main coating		1h:30 min	1h:30 min	1h:30 min
Hardness (GPa)		30 ± 2	32 ± 2	30 ± 2
Young's modulus (GPa)		290 ± 9	306 ± 7	290 ± 13
Elastic strain to failure (H/E)		0.10	0.10	0.10
Surface roughness (nm)		19.3	10.8	43.1
Grain size (nm)		26.8	32.8	36.2
Chemical composition of coatings (at.%)	N	46.8	46.5	44.8
	Al	13.3	12.1	10.5
	Si	10.1	8.9	9.1
	Ar	0.7	0.5	0.6
	Ti	29.1	27.2	24.0
	V	0	4.8	11.0
	(Ti+Al+Si+V)/N	1.12	1.14	1.22

5.3 W/cm^2 to the Cr target, adjusting the deposition pressure at the value of 0.3 Pa and the pulsed bias voltage of −80 V applied on the substrates for 5 min. Whereas, the gradient layer was deposited by applying a power density of 6.7 W/cm^2 to the Ti target, progressively decreasing the power applied to the Cr target until switching off, and increasing of the N flow progressively each minute form 0 up to 45 sccm for 5 min, adjusting the final deposition pressure to 0.5 Pa. Then, the final films were immediately deposited after the gradient layer. The deposition time of the main coatings was fixed to 1 h and 30 min for all coatings. A summary of the deposition conditions and some of the properties of the coatings is provided in Table 1.

Cross-section and surface morphologies as well as the thickness of the coatings were analysed by scanning electron microscopy (SEM). The chemical composition was assessed by energy dispersive x-ray spectroscopy (EDS).

The states of the chemical bonds of the as-deposited and oxidized coatings were evaluated using X-Ray Photoelectron Spectroscopy (XPS). The analysis was carried out with a monochromatic Al Kα X-ray source (1486.7 eV), operating at 15 kV (90 W), in FAT (Fixed Analyzer Transmission) mode, with a pass energy of 40 eV for the region ROI and 80 eV for the survey. Prior the analysis, an erosion cleaning of the surface was performed for 45 min to avoid the surface contamination of the samples. The effect of the electric charge was corrected using the carbon peak (285.0 eV) as reference. The peaks of spectra were fitted using Gaussian–Lorentzian peak shape and shirley type of the background subtraction.

The structure of the films was studied by x-ray diffraction (XRD) using Co Kα radiation (1.789010 Å) equipment, acquired in conventional mode for as deposited coatings and in grazing mode for oxidized ones in 2θ range of 15°–80°.

The hardness (H) and the reduced Young's modulus (E) of the coatings were measured by nano-indentation using a Berkovich diamond indenter. The indentation depth was <10% of the films thickness, to eliminate the substrate contribution. The tests were carried out with an applied load of 15 mN. A total of 16 measurements for each sample were performed.

The scratch tests were performed using scratch tester apparatus equipped by increasing the force from 5 to 70 N linearly, with a scratch speed of 10 mm/min and loading speed of 100 N/min. Then, the scratch tracks were demonstrated in an optical microscope and the critical load values were identified according to the standard critical loads evaluation [27], as follows: i) Lc1—first coating cracking, ii) Lc2—first coating

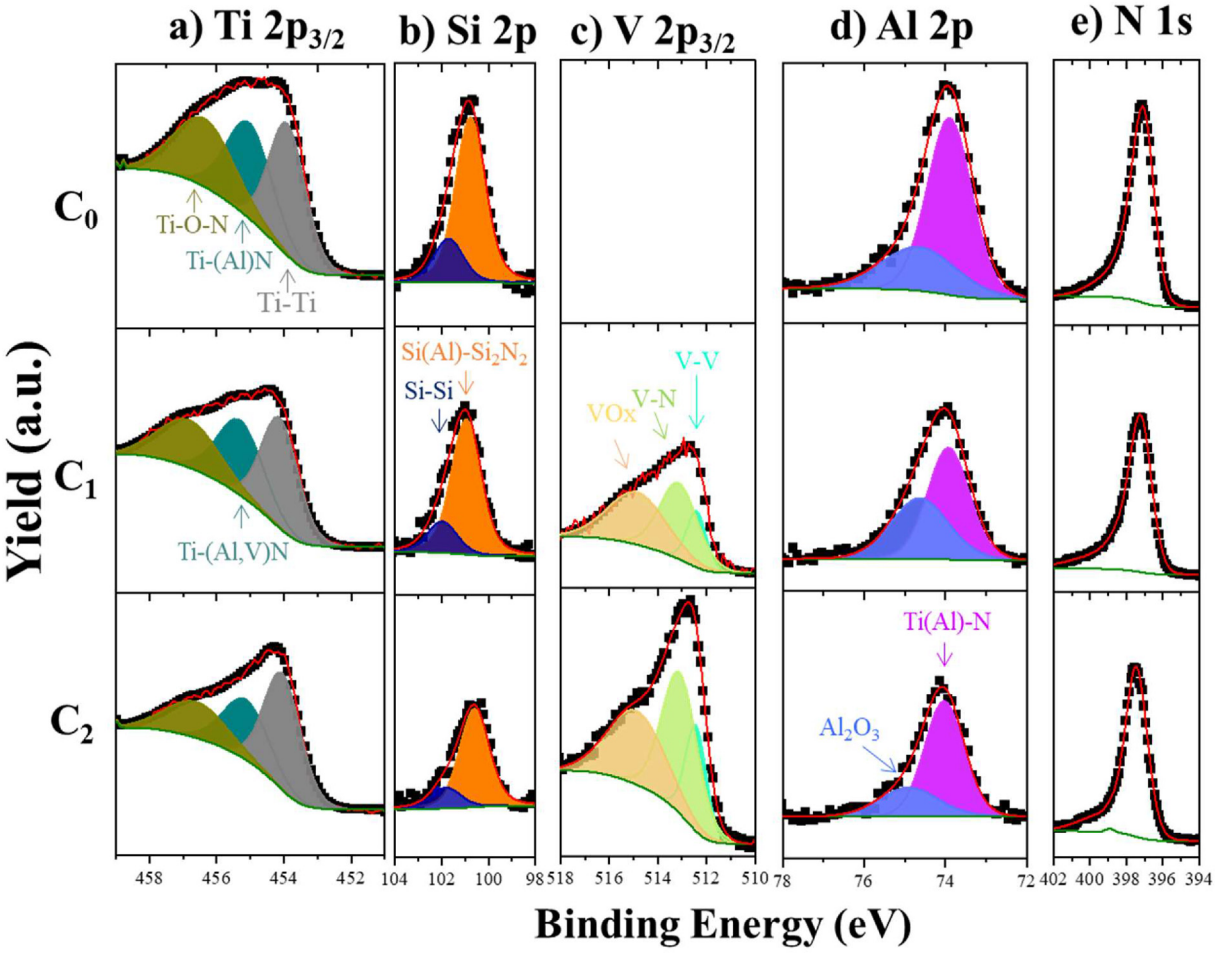

Fig. 1 – XPS core-level spectra of Ti 2p$_{3/2}$, Si 2p, V 2p$_{3/2}$, Al 2p, and N 1s of as deposited coatings. The green curve represents the background correction.

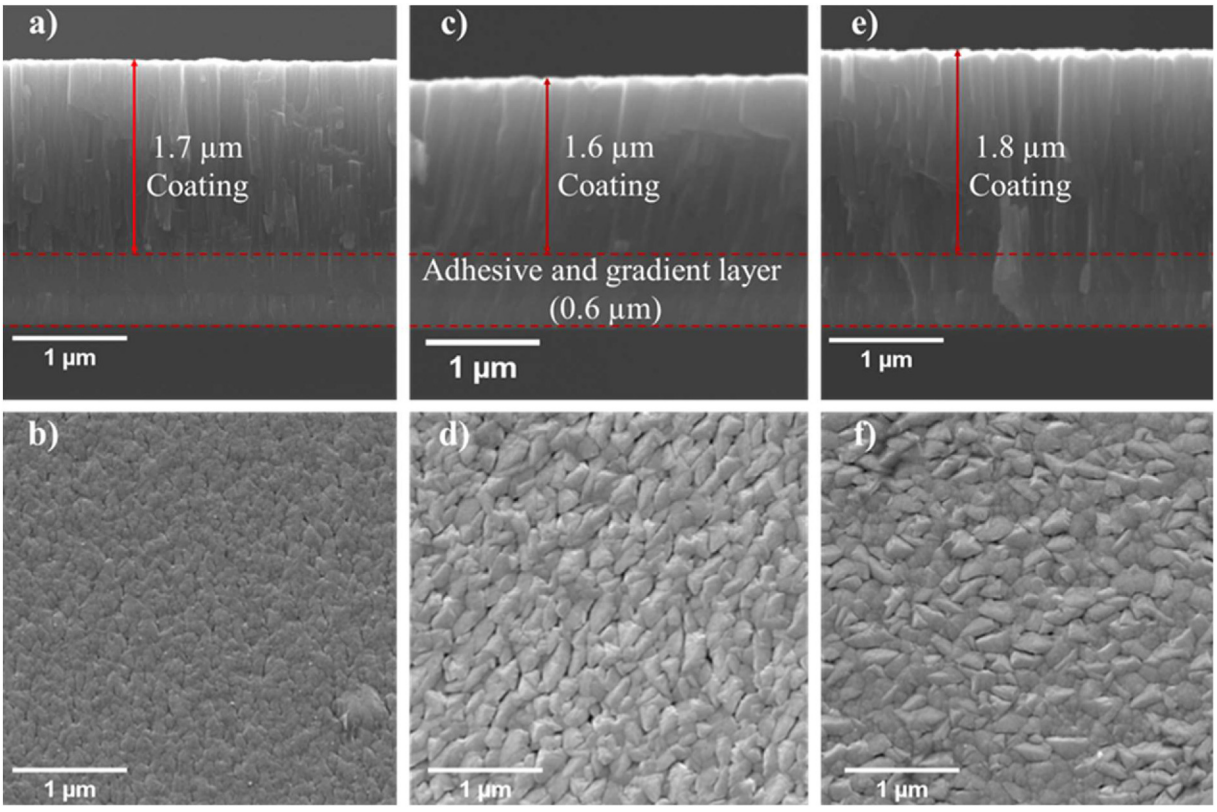

Fig. 2 – Cross-section and surface morphology of C_0 (a and b), C_1 (c and d), and C_2 (e and f).

chipping and iii) Lc3—more than half of the substrate exposure.

The effect of the V alloying on the onset point of oxidation and the oxidation resistance was studied by thermogravimetric analysis (TGA). The onset point of oxidation of each film was determined by heating the films from room temperature up to 1200 °C with a constant temperature ramp of 20 °C/min, using 50 ml/min of 99.99% purity air. The oxidation weight gain was measured at a regular 2 s intervals in a microbalance with an accuracy of 0.01 mg. Based on the dynamic oxidation curves, isothermal oxidation tests were performed in air atmosphere at 950 °C for 2 h for the reference coating, and at 700 °C for 30 min for the vanadium congaing coatings.

3. Results and discussion

3.1. *Chemical composition and elemental bonding*

The chemical composition of the coatings is presented in Table 1. As expected, the incorporation of 3 and 6 V rods to the Ti target leads to an increase of V concentration in the coatings from 4.8 at.% to 11.0 at.%, whereas the Ti concentration is decreased in the coatings. The progressive increase of the metallic-to-N element ratio (Ti +Al+ Si+V)/N suggests that sub-stoichiometric coatings are being produced, with N concentration in the range of 44.8–46.8 at.% in the coatings. The decrease in Ti and Al content with increasing vanadium incorporation into the coatings suggests the presence of Al and V as solid solution in the TiN crystal lattice by the substitution of the Ti atoms as reported by several authors [22,28,29].

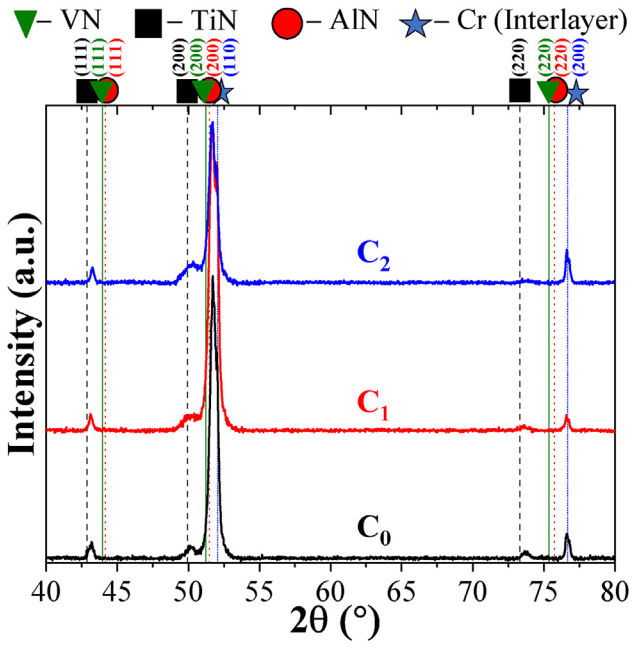

Fig. 3 – XRD diffraction patterns of the as deposited coatings obtained in the conventional mode.

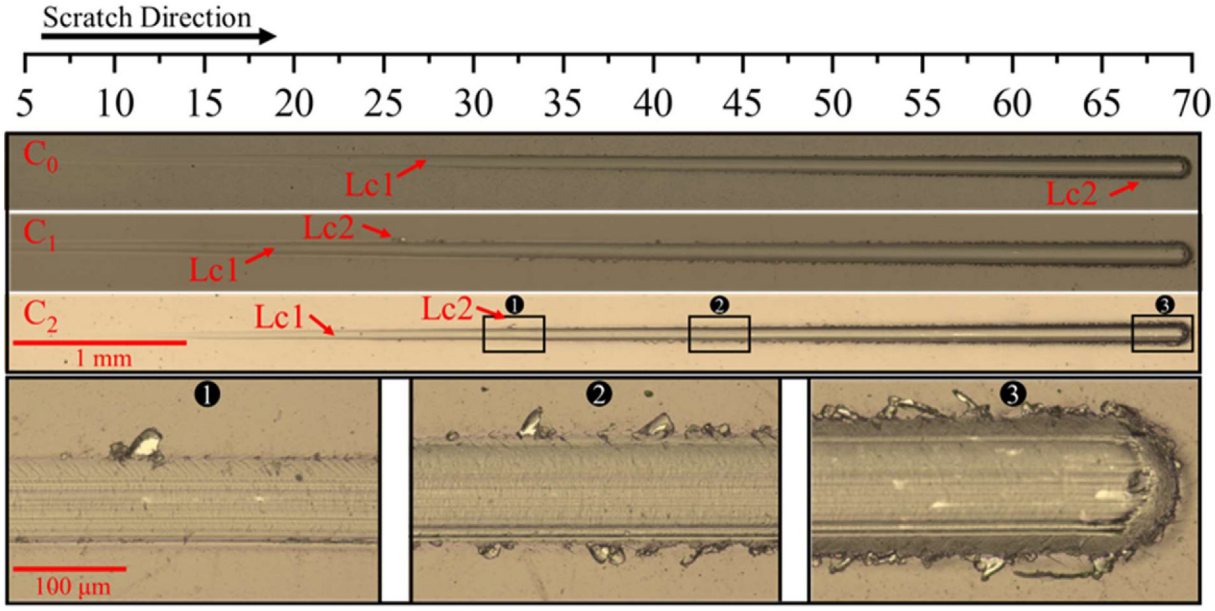

Fig. 4 – Optical microscope images of the scratch tests carried out for C_0, C_1, and C_2 films deposited onto M_2 stainless steel substrates, in the load range of 5–70 N.

The XPS core-level spectra of Ti $2p_{3/2}$, Si 2p, V $2p_{3/2}$, Al 2p, and N 1s of as deposited coatings are shown in Fig. 1. Despite of the erosion cleaning of samples' surfaces prior the XPS analysis to avoid the surface contamination, a 12–16 at.% of O is detected in all spectra, which emphasizes the existence of O in the coatings. This is due to the base pressure of the chamber, but it can be eliminated by achieving better vacuum in the chamber.

The Ti $2p_{3/2}$ core level is shown in Fig. 1a, three peak contributions centred at the binding energies of 453.9 eV, 455.0 eV and 456.4 eV are corresponded to the metallic Ti–Ti, Ti-(Al)N, Ti–O–N, respectively [30,31]. It is very clear that the sub-stoichiometry of the coatings directly influences the formed chemical bonds between elements. That is the shortage of N in the chamber leads to the formation of the metallic Ti–Ti, Si–Si and V–V bonds. The existence of Ti-(Al)N bonds in the case of reference coating and Ti-(Al,V)N bonds in the V-containing coatings support the existence of Al and V as solid solution in the TiN crystal lattice by the substitution of the Ti atoms as discussed earlier.

The fitted Si 2p core level of the coatings is shown in Fig. 1b. It can be deconvoluted into two peaks. The peaks centred at energies of 100.8 eV, 101.7 eV are associated to the SiTi(Al)–Si_2N_2, and metallic SiNx bonds, respectively [33,34].

The V $2p_{3/2}$ core level spectra of V-containing coatings (C_1, and C_2) are presented in Fig. 1c. Three peaks cantered at 512.4 eV, 513.1 eV, and 514.9 eV are the metallic V–V, V–N, and VOx, respectively [15]. The later VOx reveals the formation of vanadium oxides with insufficient amount of oxygen. Fig. 1d shows the core level spectra of Al 2p with two peaks centred at 73.9 eV and 74.7 eV, which corresponds to AlN and Al–O, respectively [9,31,32].

Finally, the N 1s core level spectra of the samples shown in Fig. 1e. (not fitted) reveals several peaks attributed to metals nitrides and oxynitrides [30,31].

3.2. *Cross-section and surface morphology*

The cross-section and surface morphologies of the coatings structure are shown in Fig. 2. The TiAlSiN reference coating (C_0) shows a dense and compact columnar growth extending from the adhesive layer to the top surface of the film (Fig. 2a). The morphology of the top surface of this columnar growth displays small features corresponds to the end of the columns, without any visible avoid (spaces) between neighbouring columns (Fig. 2b). The Coating with 4.8 at.% V concentration (C_1) exhibits a more compact coating than the reference one due to the increasing of the number of nucleation sites promoted by the V addition (see Fig. 2c and d). This explains the decrease of the deposition rate of C_1. However, increasing the V concentration to 11.0 at.% (C_2) leads to a decrease in the size of the columns irregular features, and consequently, the roughness as shown in Fig. 2d and f. The deposition rates of C_0, C_1, and C_2 are 18.9, 17.8, and 20 nm/min, respectively. Producing more compact and dense coating in the case of C_1 can explain the decrease of its deposition rate, whereas the increase of the deposition rate of C_2 is due to the higher content of V, which has higher sputtering yield than Ti [35].

3.3. *Structure*

The XRD patterns of the as-deposited TiAlSi(V)N coatings are presented in Fig. 3. The reference C_0 coating exhibits an intense diffraction peak located at 2θ of ~43.2° in between the TiN (111) (ICCD card No. 87–0633) and AlN (111) (ICCD card No. 25–1495). This structure could be identified as the cubic B1 NaCl structure with (111) preferential orientation. However, the position of the diffraction peak in-between the TiN and AlN reference cards suggests the presence of Al in solid solution in the TiN crystal lattice as reported in several studies [28,29,36]. With V addition, no significant changes or broadening are observed in the

spectra of the main diffraction peaks. Moreover, the main convolution of the VN (ICCD card No. 35–0768) peaks locates in between TiN and AlN peaks. This also suggests that the smaller sizes of Al and V atoms are incorporated into the TiN lattice and forms Ti(Al,V)N solid solution [9,35]. Si–N crystalline phase is absent in the XRD diffraction peaks due to the amorphous character as reported in the literature [31,32,37] or due to the formation of SiTix as discussed earlier in XPS analysis. For example, Houska et al. [38] reported that the maximum Si content able to be incorporated onto the TiN lattice is around 4 at.%, whilst Patscheider et al. [37] reported that TiSiN coatings with Si contents (>10 at.%) exhibit low crystallinity with very broad diffraction peaks. Therefore, the Si–N phase with the Si content range of 8.9–10.1 at% in our coatings is amorphous or quasi-amorphous.

3.4. *Mechanical properties*

3.4.1. *Hardness (H) and reduced Young's modulus (E) of as-deposited coatings*

H and E values of the coatings are presented in Table 1. The coating with 4.8 at% of V content C_1 shows the highest values of H and E as 32 GPa and 306 GPa, respectively. As shown in Table 1, C_1 exhibits the lowest value of surface roughness (10.8 nm), which shows the benefit of a denser and finer columnar structure of the coating on the improvement of the mechanical properties such as H and E [35]. In addition, the hardening of coatings is mostly results from the nitride lattice distortion, that improves the resistance to plastic deformation (solid solution hardening) as reported in different coating systems that contain vanadium (TiAlVN [10] and Ti–Si–V–N [4]). Residual stresses should not be a factor of hardness differentiation between the coatings because all coatings have approximately the same level of compressive residual stresses (2–3 GPa).

3.4.2. *Adhesion critical loads*

Fig. 4 shows the adhesion scratch micrographs for C_0, C_1, and C_2 coatings. All coatings show a good adhesion to the substrates. The reference coating (C_0) displays the highest values of the adhesion critical load values of 27 N and 67 N of – Lc1 and - Lc2, respectively. These critical loads are decreased with V addition, i.e. C_1 with V content of 4.77 at.% shows the to the lowest values of Lc1 (18 N) and Lc2 (26 N) whereas the values are increased to Lc1 (22 N) and - Lc2 (32 N) for C_2 with the highest V content for C_1 with V content of 4.77 at.%. None of the three coatings shows Lc3 failure until the end of the test, revealing the good adhesin to the substrates.

3.5. *Oxidation resistance*

The thermogravimetric oxidation curves of the three coatings performed at a constant linear temperature ramp from room temperature to 1200 °C, and their isothermal TG curves exposed at chosen temperatures and times are displayed in Fig. 5. The onset point of oxidation temperature of reference coating is around ~940 °C, whilst for the V containing coatings it decreases significantly down to a temperature of approximately 720 °C and 640 °C for C_1 and C_2, respectively, and it strongly depends on the V concentration in the coatings. This

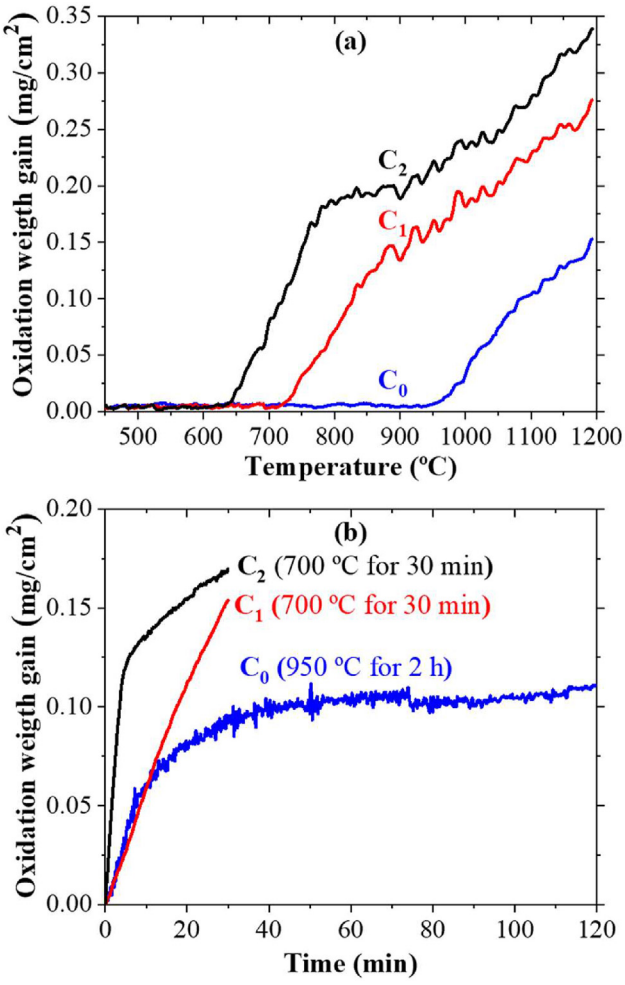

Fig. 5 – a) Thermogravimetric oxidation rate of C_0, C_1 and C_2 performed at a constant linear temperature ramp from RT to 1200 °C at a rate of 20 °C/min, and b) the isothermal TG curves of coatings exposed at chosen temperatures and times as indicated in the legend of the image.

corroborates our previous work where the addition of V to the nanocomposite TiSiN films affects the starting points of oxidation [4]. However, these points are lower than the ones of the current work.

The reference C_0 coating starts to oxidize at ~940 °C. After this temperature, the mass gain increases exponentially in the temperature range of 940 °C - 1200 °C up to the final weight gain of 0.15 mg/cm^2. This low oxidation weight gain corroborates well the cross-section and surface morphology of the coating as shown in Fig. 6a and b, where an oxidized zone of the coating can be distinguished from the non-oxidized zone. Despite the final temperature the TGA test is very high (1200 °C), only 52% of the total thickness of the coating is oxidized. It exhibits a typical parabolic oxidation weight gain as a function of time indicating the formation of protective Si and Al-rich oxide layer (Fig. 5b). Contrary, the oxides mass gain of V containing coatings C_1 and C_2 is much higher and have a linear oxidation rate range of the curve due to the formation of a non-protective oxides V–O [4]. In fact, the weight oxidation gain curves evolution of these two coatings

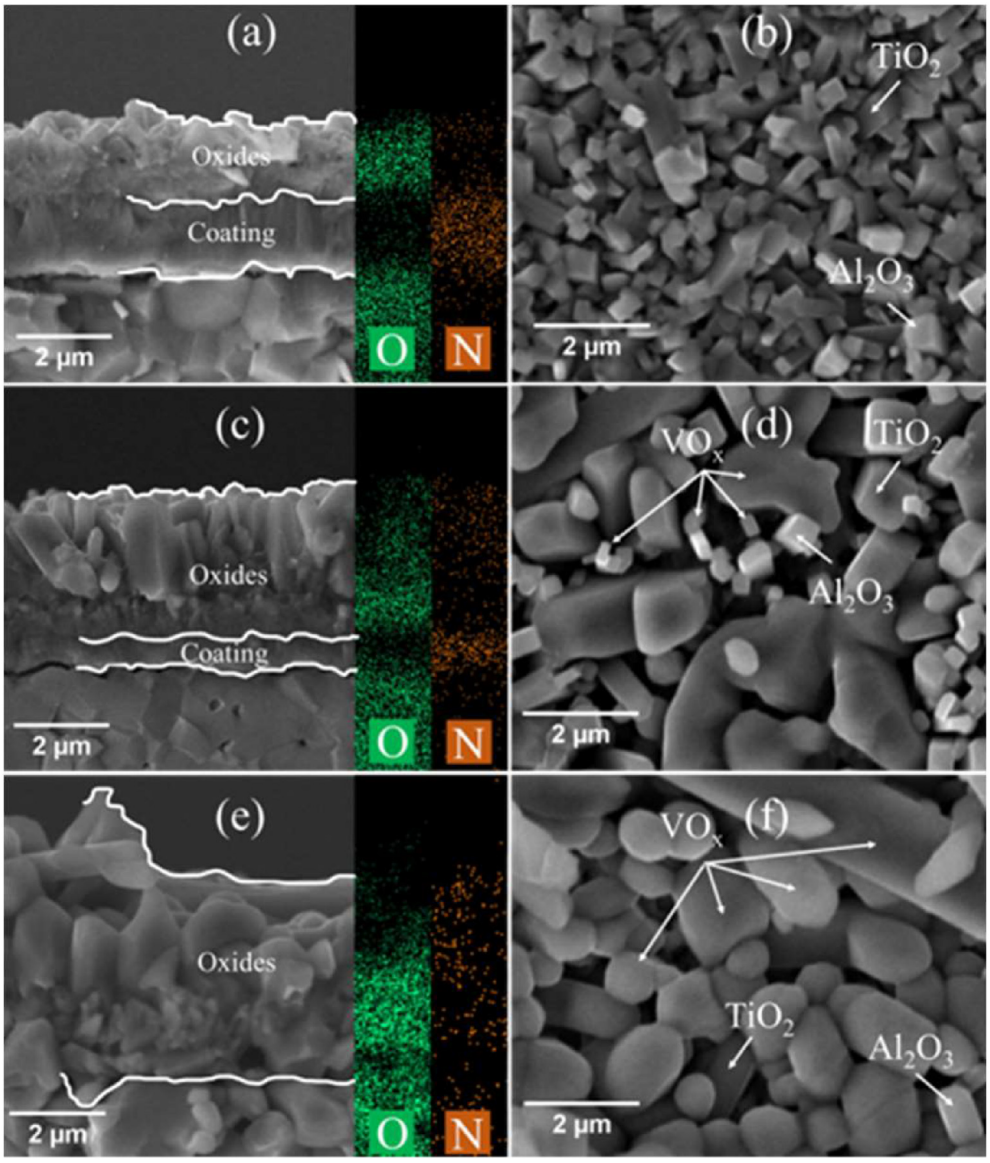

Fig. 6 – Cross-section morphology of C_0, C_1, and C_2 coatings after continuous oxidation up to 1200 °C with corresponding oxygen and N elemental maps and surface morphologies.

reveals much higher values than the reference coating, i.e., an 85% of the total thickness of C_1 is oxidized after the test (Fig. 6c and d), whereas the coating with the highest V (C_2) is totally oxidized (Fig. 6e and f). Moreover, their isothermal curves tested at 700 °C shows two stages of oxidation mass gain: at the first step, the weight gain increases rapidly (almost linear increase) up to approximately 0.12 mg/cm^2, and then changes to a parabolic law. The isothermal annealing of C_2 shows significant increase of the mass gain and follows the parabolic evolution (Fig. 5b).

The cross-section and surface morphology of the isot-hermal oxidation tests at 950 °C for 2 h for the reference coating (C_0) and at 700 °C for 30 min for C_1 and C_2 are shown in Fig. 7. In agreement with the dynamic oxidation tests, the reference coating C_0 reveals the best oxidation resistance and shows a thinnest dual oxides layer: an outer porous Ti–Al–O rich layer with plate like crystals on the top and, underneath, an inner Ti–Si–O rich layer with Al depletion, as suggested by the elemental distribution maps shown in Fig. 8. The top layer of the plate like crystals have been classified by XRD (Fig. 9) together with eds mapping to the two main oxide phases: TiO_2 (rutile ICCD card Nº. 01-76-0649 and anatase ICCD card Nº. 01-071-1166) phases on the top surface, and Al_2O_3 (ICCD card Nº. 00-002-1373) phase underneath. The same types of these oxides were reported for the reference coating presented in our previous work [39]. The only difference between the two coatings is that the one presented in this work shows distinguishable TiO_2 (top) and Al_2O_3 (underneath) layers while, the one presented in the previous work shows a mixture of these phases. The inner Ti–Si–O is also identified based on the elemental map distributions as a mixture of Si–O and Ti–Si–O oxide phases. However, these phases could not be detected by the XRD due to their amorphous structure [20,40]. During the oxidation process, Ti and Al diffuse outwards and react with O

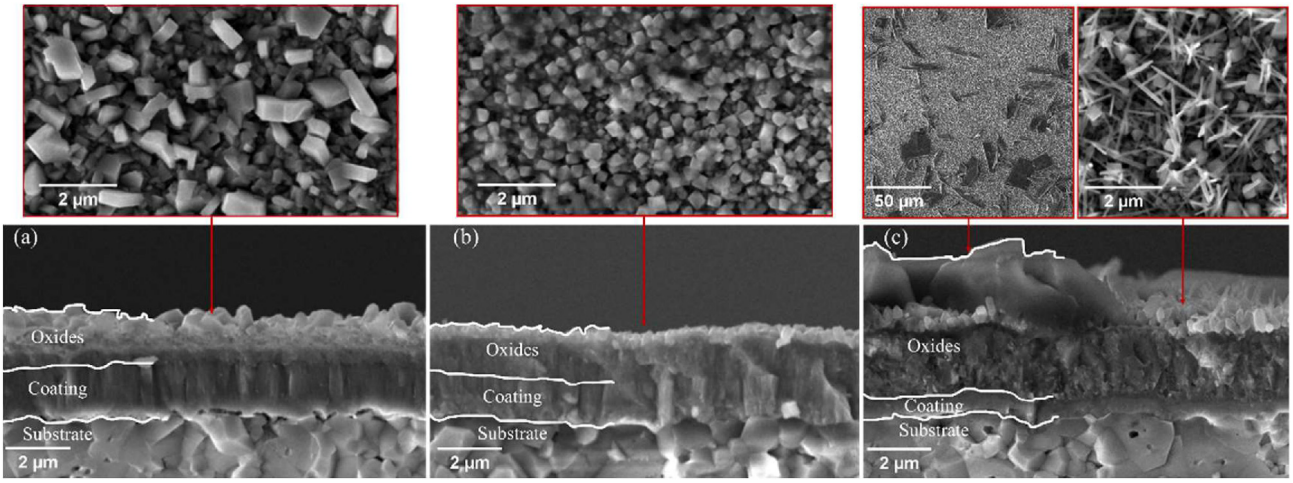

Fig. 7 – Cross-section and surface morphology of C_0 coating after oxidation at 950 °C for 2 h, and C_1 & C_2 coatings after oxidation at 700 °C for 30 min.

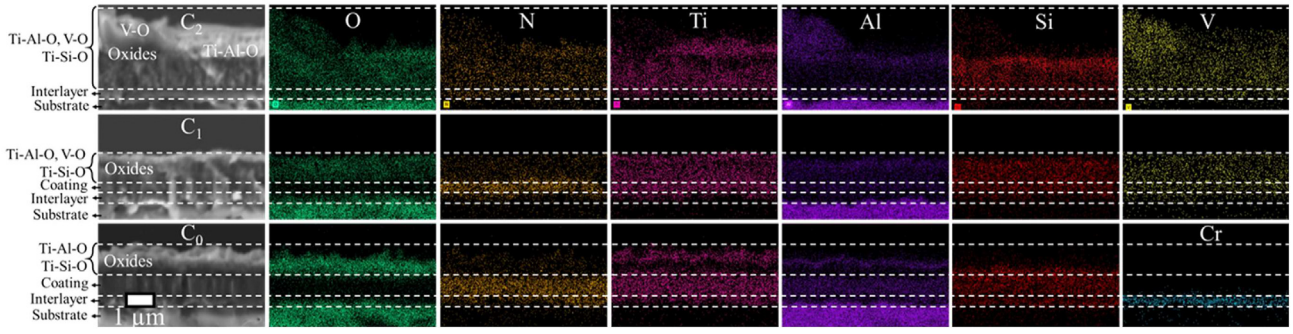

Fig. 8 – Cross-section and corresponding elemental maps distribution of C_0 coating after oxidation at 950 °C for 2 h, and C_1 & C_2 coatings after oxidation at 700 °C for 30 min.

to form TiO_2 and Al_2O_3 phases, whilst O diffuses inwards and forms the Ti–Si–O rich layer below the top layer. After the formation of these oxides on the top, the coating becomes more protected from any farther in-depth oxidation due to the protective Al_2O_3, Ti–Si–O, and Si–O protective oxides that works as a good barrier against any inward O diffusion.

V addition degrades the oxidation resistance of the coatings, and a higher thickness of oxide scale is formed (Fig. 7 b and c), which leads to a different morphology of oxides. Indeed, the oxide scale thickness is increased with increasing the V- concentration in the coatings. Despite the existence of Ti–Si–O and Ti–Al–O layers in V-alloyed coatings as similar order of the reference coating, two main differences could be notice in the oxide scale: i) in the case of the coating with low V concentration (C1), Ti–Al–O layer shows a mixture TiO_2, Al_2O_3, V_2O_3 and VO_2 phases as confirmed from elemental eds mapping (Fig. 8) and XRD (Fig. 9), confirming the dominant out diffusion of V to the surface, which leads to changes on the surface morphology. These changes are associated with the melting of V_2O_5, that originates a smoother surface and decreases the size of plate like features compared with the reference coating (C_0) as shown in Fig. 7. However, two different zones of surface morphology could be distinguished in the case of higher V concentration in the coating (C_2), i.e., a

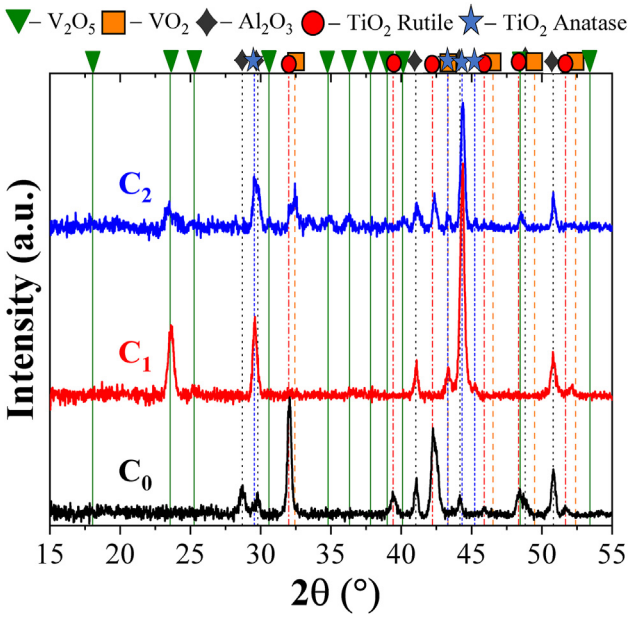

Fig. 9 – XRD diffraction patterns acquired in grazing incidence mode for C_0 coating after oxidation at 950 °C for 2 h, and C_1 & C_2 coatings after oxidation at 700 °C for 30 min.

continues V–O layer zone, and the zone of TiO_2, Al_2O_3, V_2O_3 and VO_2 oxides mixture with V richer oxides. This is corresponding to the needle-like structure shown in Fig. 7c. ii) no anatase TiO_2 phase were detected in the oxidized V-containing coating due to the lower annealing temperature, that is the possibility of formation of this oxide phase is very low at annealing temperature lower than 900 °C [41].

4. Conclusions

In this work, the influence of V addition on the morphology, structure, hardness (H) and reduced Young's modulus (E), adhesion, and oxidation resistance of TiAlSiN coatings is investigated. The coatings were produced by DC reactive magnetron sputtering, with increasing V contents from 0, 4.8, and 11.0 at.%. All coatings exhibit a fcc type structure. However, the position of the diffraction peak in-between the TiN and AlN reference cards suggests the presence of Al in solid solution in the TiN crystal lattice. No significant changes or broadening are observed in the spectrum of the main diffraction with V addition. However, the main convolution of the VN peaks locates in between TiN and AlN peaks, suggesting the smaller sizes of Al and V atoms are incorporated into the TiN lattice and forms Ti(Al,V)N solid solution. The coating with 4.8 at.% V content shows the highest H and E values, whereas the values decrease with the highest V concentration and shows a similar value of the reference coating. All coatings adhere well to the substrates and exhibit a dense and compact columnar growth extending from the adhesive layer to the top surface of the coatings. The dynamic thermal gravimetric oxidation curves reveal that V additions decreases the onset point of oxidation significantly and degrades the oxidation resistance of the coatings. A dual oxide layer is formed on the top surface of the reference coating: an outer porous Ti–Al–O rich layer with plate like features on the top, which classified to TiO_2 (rutile and anatase) and Al_2O_3 phase, and an inner Ti–Si–O rich layer with Al depletion that identified as mixture of amorphous Si–O and Ti–Si–O protective oxides. The diffusion kinetics of V governs the oxidation behaviour of V containing coatings, i.e. the higher the V concentration is, the easier the disruption of the formation of the protective continuous oxide layers.

Declaration of Competing Interest

The authors declare that they have no known competing financial interests or personal relationships that could have appeared to influence the work reported in this paper.

Acknowledgements

This research is sponsored by national funds through FCT – Fundação para a Ciência e a Tecnologia, under the projects: UIDB/00285/2020, SMARTLUB—ref. "POCI-01-0145-FEDER-031-807". MCTool21 project "Manufacturing of cutting tools for the 21st century: from nano-scale material design to numerical process simulation" (reference: POCI-01-0247-FEDER-045940), co-financed by the European Regional Development Fund, through Portugal 2020 (PT2020), and by the Competitiveness and Internationalization Operational Programme (COMPETE 2020).

REFERENCES

[1] Magnéli A. Structures of the ReO_3-type with recurrent dislocations of atoms: 'homologous series' of molybdenum and tungsten oxides. Acta Crystallogr 1953;6:495–500. https://doi.org/10.1107/s0365110x53001381.
[2] Franz R, Mitterer C. Vanadium containing self-adaptive low-friction hard coatings for high-temperature applications: a review. Surf Coating Technol 2013;228:1–13. https://doi.org/10.1016/j.surfcoat.2013.04.034.
[3] Fateh N, Fontalvo GA, Gassner G, Mitterer C. Influence of high-temperature oxide formation on the tribological behaviour of TiN and VN coatings. Wear 2007;262:1152–8. https://doi.org/10.1016/j.wear.2006.11.006.
[4] Fernandes F, Loureiro A, Polcar T, Cavaleiro A. The effect of increasing V content on the structure, mechanical properties and oxidation resistance of Ti – Si–V–N films deposited by DC reactive magnetron sputtering. Appl Surf Sci 2014;289:114–23. https://doi.org/10.1016/j.apsusc.2013.10.117.
[5] Torres H, Rodríguez Ripoll M, Prakash B. Tribological behaviour of self-lubricating materials at high temperatures. Int Mater Rev 2018;63:309–40. https://doi.org/10.1080/09506608.2017.1410944.
[6] Voevodin AA, Muratore C, Aouadi SM. Hard coatings with high temperature adaptive lubrication and contact thermal management: review. Surf Coating Technol 2014;257:247–65. https://doi.org/10.1016/j.surfcoat.2014.04.046.
[7] Wu Z, Tang P, Wu Y, Wang Q, Qi Z. Wear behavior of AlCrSiVN coatings at elevated temperature up to 700 °C. Vacuum 2019;169:108876. https://doi.org/10.1016/j.vacuum.2019.108876.
[8] Franz R, Neidhardt J, Mitterer C, Schaffer B, Hutter H, Kaindl R, et al. Oxidation and diffusion processes during annealing of AlCrVN hard coatings. J Vac Sci Technol Vac Surf Films 2008;26:302–8. https://doi.org/10.1116/1.2841508.
[9] Lin J, Wei R, Ge F, Li Y, Zhang X, Huang F, et al. TiSiCN and TiAlVSiCN nanocomposite coatings deposited from Ti and Ti-6Al-4V targets. Surf Coating Technol 2018;336:106–16. https://doi.org/10.1016/j.surfcoat.2017.10.009.
[10] Tillmann W, Momeni S, Hoffmann F. A study of mechanical and tribological properties of self-lubricating TiAlVN coatings at elevated temperatures. Tribol Int 2013;66:324–9. https://doi.org/10.1016/j.triboint.2013.06.007.
[11] Panjan P, Drnovšek A, Kovač J, Čekada M, Panjan M. Oxidation processes in vanadium-based single-layer and nanolayer hard coatings. Vacuum 2017;138:230–7. https://doi.org/10.1016/j.vacuum.2016.12.025.
[12] Xu J, Chen J, Yu L. Influence of Si content on the microstructure and mechanical properties of VSiN films deposited by reactive magnetron sputtering. Vacuum 2016;131:51–7. https://doi.org/10.1016/j.vacuum.2016.05.030.
[13] Bondarev AV, Kvashnin DG, Shchetinin IV, Shtansky DV. Temperature-dependent structural transformation and friction behavior of nanocomposite VCN- (Ag) coatings. Mater Des 2018;160:964–73. https://doi.org/10.1016/j.matdes.2018.10.029.
[14] Fernandes F, Morgiel J, Polcar T, Cavaleiro A. Oxidation and diffusion processes during annealing of TiSi(V)N films. Surf

Coating Technol 2015;275:120–6. https://doi.org/10.1016/j.surfcoat.2015.05.031.
[15] Restrepo J, Mondragon-Rodriguez G, Gonzalez-Carmona JM, Alvarado-Orozco JM, Garcia-Zarco O, Rodil SE. Cathodic arc evaporation of self-lubricating TiSiVN coatings. J Mater Eng Perform 2021;32. https://doi.org/10.1007/s11665-021-06333-8.
[16] Fernandes F, Oliveira JC, Cavaleiro A. Self-lubricating TiSi(V)N thin films deposited by deep oscillation magnetron sputtering (DOMS). Surf Coating Technol 2016;308:256–63. https://doi.org/10.1016/j.surfcoat.2016.07.039.
[17] Fernandes F, Polcar T, Cavaleiro A. Tribological properties of self-lubricating TiSiVN coatings at room temperature. Surf Coating Technol 2015;267:8–14. https://doi.org/10.1016/j.surfcoat.2014.10.016.
[18] Helmersson U, Todorova SS, Barnett SA, Sundgren J-E, Markert LC, Greene JE. Growth of single-crystal TiN/VN strained- layer superlattices with extremely high mechanical hardness. J Appl Phys 2003;62:481. https://doi.org/10.1063/1.339770.
[19] Al-Rjoub A, Cavaleiro A, Fernandes F. Structure, morphology, thermal stability and oxidation resistance of multilayered TiSiN/VN films: influence of TiSiN-layer thickness. J Mater Eng Perform 2021:1059–9495. https://doi.org/10.1007/s11665-021-05560-3.
[20] Athmani M, AL-Rjoub A, Cavaleiro D, Chala AA, Cavaleiro, Fernandes F. Microstructural, mechanical, thermal stability and oxidation behavior of TiSiN/CrVxN multilayer coatings deposited by D.C. reactive magnetron sputtering. Surf Coating Technol 2021;405:126593. https://doi.org/10.1016/j.surfcoat.2020.126593.
[21] Chang Y, Chiu W, Hung J. Mechanical properties and high temperature oxidation of CrAlSiN/TiVN hard coatings synthesized by cathodic arc evaporation. Surf Coating Technol 2016;303:18–24. https://doi.org/10.1016/j.surfcoat.2016.02.047.
[22] Zhang J, Chen L, Kong Y. The microstructural, mechanical and thermal properties of TiAlVN, TiAlSiN monolithic and TiAlVN/TiAlSiN multilayered coatings. J Alloys Compd 2022;899:163332. https://doi.org/10.1016/j.jallcom.2021.163332.
[23] Mayrhofer PH, Hovsepian PE, Mitterer C, Münz WD. Calorimetric evidence for frictional self-adaptation of TiAlN/VN superlattice coatings. Surf Coating Technol 2004;177–178:341–7. https://doi.org/10.1016/j.surfcoat.2003.09.024.
[24] Lewis DB, Creasey S, Zhou Z, Forsyth JJ, Ehiasarian AP, Hovsepian PE, et al. The effect of (Ti+Al):V ratio on the structure and oxidation behaviour of TiAlN/VN nano-scale multilayer coatings. Surf Coating Technol 2004;177–178:252–9. https://doi.org/10.1016/j.surfcoat.2003.09.041.
[25] Zhou Z, Rainforth WM, Rodenburg C, Hyatt NC, Lewis DB, Hovsepian PE. Oxidation behavior and mechanisms of TiAlN/VN coatings. Metall Mater Trans A Phys Metall Mater Sci 2007;38:2464–78. https://doi.org/10.1007/s11661-007-9293-4.
[26] Franz R, Neidhardt J, Kaindl R, Sartory B, Tessadri R, Lechthaler M, et al. Influence of phase transition on the tribological performance of arc-evaporated AlCrVN hard coatings. Surf Coating Technol 2009;203:1101–5. https://doi.org/10.1016/j.surfcoat.2008.10.003.
[27] Jacobs R, Meneve J, Dyson G, Teer DG, Jennett NM, Harris P, et al. A certified reference material for the scratch test. Surf Coating Technol 2003;174–175:1008–13. https://doi.org/10.1016/S0257-8972Ž03.00470-5.
[28] Carvalho S, Rebouta L, Cavaleiro A, Rocha LA, Gomes J, Alves E. Microstructure and mechanical properties of nanocomposite (Ti, Si, Al)N coatings. Thin Solid Films 2001;398–399:391–6. https://doi.org/10.1016/S0040-6090(01)01348-7.
[29] Zhang K, Xin L, Lu Y, Cheng Y, Wang X, Zhu S, et al. Improving oxidation resistance of γ-TiAl based alloy by depositing TiAlSiN coating: effects of silicon. Corrosion Sci 2021;179:109151. https://doi.org/10.1016/j.corsci.2020.109151.
[30] Rose F, Marchon B, Rawat V, Pocker D, Xiao Q-F, Iwasaki T. Ultrathin TiSiN overcoat protection layer for magnetic media. J Vac Sci Technol Vac. Surf. Films 2011;29:051502. https://doi.org/10.1116/1.3607423.
[31] AL-Rjoub A, Rebouta L, Cunha NF, Fernandes F, Barradas NP, Alves E. W/AlSiTiNx/SiAlTiOyNx/SiAlOx multilayered solar thermal selective absorber coating. Sol Energy 2020;207:192–8. https://doi.org/10.1016/j.solener.2020.06.094.
[32] Barshilia HC, Ghosh M, Shashidhara, Ramakrishna R, Rajam KS. Deposition and characterization of TiAlSiN nanocomposite coatings prepared by reactive pulsed direct current unbalanced magnetron sputtering. Appl Surf Sci 2010;256:6420–6. https://doi.org/10.1016/j.apsusc.2010.04.028.
[33] AL-Rjoub A, Costa P, Rebouta L, Cerqueira MF, Alpuim P, Barradas NP, et al. Characterization of magnetron sputtered sub-stoichiometric CrAlSiNx and CrAlSiOyNx coatings. Surf Coating Technol 2017;328:134–41. https://doi.org/10.1016/j.surfcoat.2017.08.038.
[34] Finster J, Klinkenberg ED, Heeg J, Braun W. ESCA and SEXAFS investigations of insulating materials for ULSI microelectronics. Vacuum 1990;41:1586–9. https://doi.org/10.1016/0042-207X(90)94025-L.
[35] Wang CF, Ou SF, Chiou SY. Microstructures of TiN, TiAlN and TiAlVN coatings on AISI M2 steel deposited by magnetron reactive sputtering. Oral Oncol 2014;50:2559–65. https://doi.org/10.1016/S1003-6326(14)63383-5.
[36] Feng C, Zhu S, Li M, Xin L, Wang F. Effects of incorporation of Si or Hf on the microstructure and mechanical properties of Ti-Al-N films prepared by arc ion plating (AIP). Surf Coating Technol 2008;202:3257–62. https://doi.org/10.1016/j.surfcoat.2007.11.036.
[37] Patscheider J, Zehnder T, Diserens M. Structure-performance relations in nanocomposite coatings. Surf Coating Technol 2001;146–147:201–8. https://doi.org/10.1016/S0257-8972(01)01389-5.
[38] Houska J, Klemberg-Sapieha JE, Martinu L. Atomistic simulations of the characteristics of TiSiN nanocomposites of various compositions. Surf Coating Technol 2009;203:3348–55. https://doi.org/10.1016/j.surfcoat.2009.04.021.
[39] AL-Rjoub A, Cavaleiro A, Bin Yaqub T, Evaristo NMFM, Fernandes F. TiAlSiN(Ag) coatings for high temperature applications: the influence of Ag alloying on the morphology, structure, thermal stability and oxidation resistance. Surf Coating Technol 2022;442:128087. https://doi.org/10.1016/j.surfcoat.2022.128087.
[40] Diserens M, Patscheider J, Le F. Mechanical properties and oxidation resistance of nanocomposite TiN − SiNx physical-vapor-deposited thin films. Surf Coating Technol 1999;121:158–65. https://doi.org/10.1016/S0257-8972(99)00481-8.
[41] Moritz Y, Saringer C, Tkadletz M, Stark A, Schell N, Letofsky-Papst I, et al. Oxidation behavior of arc evaporated TiSiN coatings investigated by in-situ synchrotron X-ray diffraction and HR-STEM. Surf Coating Technol 2020;404:126632. https://doi.org/10.1016/j.surfcoat.2020.126632.